Polymer 49 (2008) 5146–5157

Contents lists available at ScienceDirect

Polymer

journal homepage: www.elsevier.com/locate/polymer

Macroscopically oriented lamellar microdomains created by "cold zone-heating" method involving OOT☆

Kazuki Mita [a,1], Hirokazu Tanaka [a,1], Kenji Saijo [a], Mikihito Takenaka [a,b], Takeji Hashimoto [a,c,*]

[a] Department of Polymer Chemistry, Graduate School of Engineering, Kyoto University, Katsura, Nishikyo-ku, Kyoto 615-8510, Japan
[b] Structural Materials Science Laboratory, SPring-8 Center, RIKEN Harima Institute Research, Hyogo 679-5148, Japan
[c] Advanced Science Research Center (ASRC), Japan Atomic Energy Agency (JAEA), Tokai-mura, Ibaraki-Pref. 319-1195, Japan

ARTICLE INFO

Article history:
Received 25 June 2008
Received in revised form 18 August 2008
Accepted 26 August 2008
Available online 13 September 2008

Keywords:
Block copolymer
Zone heating
Order–order transition

ABSTRACT

The zone-heating method, which involves ordering of materials under moving temperature gradient ∇T, has been widely used as a technique to create macroscopically oriented ordered structures of various kinds of materials. We applied this method to a large molecular weight symmetric polystyrene-*block*-polyisoprene diblock copolymer (dibcp) at a temperature where the ∇T field exists below its order–disorder transition temperature T_{ODT} of the dibcp. In this method we first prepared the solvent-cast bulk films of the dibcp having a nonequilibrium morphology of hexagonally packed cylindrical microdomains (hex-cyl) by using a solvent selectively good for polyisoprene blocks. Then the zone-heating method was applied to the order–order transition process from the nonequilibrium hex-cyl to equilibrium lamellae. The "cold zone-heating" method, "cold" in the sense of the ∇T field existing below T_{ODT}, successfully created macroscopically oriented lamellae with their normals preferentially oriented parallel to the ∇T axis and their edges preferentially standing with respect to the bulk film surfaces. It was also found that the initial orientation of the (100) plane of hex-cyl normal to the ∇T axis prefers to that parallel to the ∇T axis for a better macroscopic alignment of lamellae. A possible model for the cold zone-heating-induced lamellar orientation will be discussed in the text.

1. Introduction

The zone-heating method has been widely used as a technique to align the macroscopic orientation of ordered structures of various kinds of materials [1]. The method applies a moving temperature gradient, ∇T, to materials during ordering process from melts to ordered structures such as crystals and ordered microdomain structures [2–5]. We have been investigating the special orientation and texture of the microdomains achieved by this method on polystyrene-*block*-polyisoprene (SI) diblock copolymers (dibcps) during their ordering process through order–disorder transition (ODT) [2–6]. The method was found to create macroscopically oriented microdomain structures for bulk dibcp films, a single crystal of lamella microdomain structure [2,3] and the columnar grain texture having a special orientation of hexagonally packed cylindrical microdomain structure (hex-cyl) [4,5].

In the zone-heating process as described above, a bulk block copolymer (bcp) sheet with 2 mm thickness, in which the bcp is initially in the ordered state without a specific orientation of microdomain structure, contacts to a glass surface set perpendicular to O*z*-axis as shown in Fig. 1. In the zone-heated part, we set the lower and higher limit of temperature T_1 and T_2 at the left and right edge, respectively, where $T_1 < T_{ODT} < T_2$. Here, T_{ODT} is the ODT temperature. Thus produced ∇T zone moved continuously from the left edge to the right edge of the sheet along O*z*-axis, giving rise to the sequential ordering from the glass surface side of the sheet toward its interior [2–5]. This sequential ordering creates macroscopically oriented microdomain structure in the bulk bcp sheet. The sequential ordering is strongly affected by the surface-induced ordering of bcps [7–12], for which the glass surface plays a role in the early stage of zone heating. In the rest of the stage, the surface of as-grown, well-aligned microdomain structure plays a role for the surface-induced ordering in place of the glass surface. In order to bring about the sequential ordering, the conditions of a large ∇T and a small moving rate R of ∇T are required so that the ordering occurs only in a supercooled disordered phase existing in a very narrow slit-like region where ordering is strongly affected by the

☆ Presented in part (Hashimoto T, Tanaka H. Japanese Patent publication 2005-060583. 2005-03-10).

* Corresponding author. Advanced Science Research Center (ASRC), Japan Atomic Energy Agency (JAEA), Tokai-mura, Ibaraki-Pref. 319-1195, Japan.
E-mail address: hashimoto@alloy.polym.kyoto-u.ac.jp (T. Hashimoto).
[1] Present address: R&D Center, Mitsui Chemicals, Inc., 580-32 Nagaura, Sodegaura, Chiba 299-0265, Japan.

0032-3861/$ – see front matter © 2008 Elsevier Ltd. All rights reserved.
doi:10.1016/j.polymer.2008.08.059

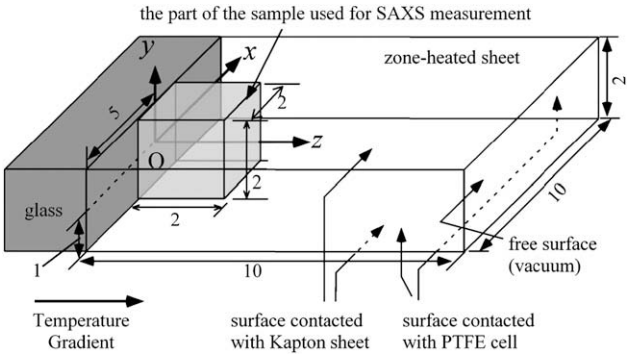

Fig. 1. Schematic diagram showing the Cartesian coordinate O*xyz* fixed to the zone-heated sheet. The origin of the Cartesian coordinate was set at the center of the glass surface. The cube shaded with light grey was cut out from the frozen zone-heated sheet for SAXS measurement. The lengths in this figure are expressed in unit of "mm".

surfaces. Otherwise, the sheet would have a wide region of supercooled disordered melt where a random nucleation and growth of microdomains will occur.

Berry et al. [13] applied their zone-heating method, which imposes the moving ∇T with the highest temperature lower than T_{ODT}, to an as-spun-cast thin film of hex-cyl forming polystyrene-*block*-poly(methylmethacrylate) (PS-*b*-PMMA), which had the vitrified disordered structure before the application of the zone-heating method, and found that their method orients the hex-cyl structure in a mesoscopic scale. Since ∇T exists below T_{ODT}, they called "cold zone heating" for the particular zone-heating method.

In our method, we need to set T_2 above T_{ODT}, in order to attain the sequential ordering of the bcp from the disordered state. Thus, it is impossible to apply the method to bcps having high degree of polymerization N, since we cannot bring such bcps into the disordered state without thermal degradation. The method of Berry et al. [13] also cannot be applied to thick sheets ($\sim$2 mm) of SI dibcps having high degree of polymerization, because it is difficult to achieve initially disordered state in the thick sheets.

In order to overcome the difficulties associated with the high-temperature zone-heating method and to induce macroscopic orientation of microdomains in bcps having high value of N, we developed the following method; we induced order–order transition (OOT) instead of ODT during our zone-heating method. It is well known that the solvent casting of bcp films with selective solvents induces nonequilibrium morphologies trapped in as-cast films [14,15]. In the case of SI dibcps with a symmetric block composition, hex-cyl of polystyrene (PS) block chains in the matrix of polyisoprene (PI) block chains can be produced by the solvent cast with cyclohexane, which is a good solvent for PI but a poor solvent for PS, at room temperature. The hex-cyl is frozen in the as-cast film due to vitrification of the PS cylinders during the solvent evaporation process [16]. This thermodynamically unstable hex-cyl, trapped in the as-cast film, transforms into the thermodynamically stable lamella by heating the as-cast films at temperatures T above the glass transition temperature (T_g) of PS ($\sim$90 °C, designated as $T_{g,PS}$). The transformation involves the process of disruptions of cylindrical interfaces and creations of lamellar interface [17], which is expected to be affected by the external field given by the moving ∇T field.

The cold zone heating at T, where $T_2 < T_{g,PS} < T < T_1 < T_{ODT}$, can induce the sequential OOT in the dibcp bulk, so that macroscopically oriented lamella is expected to be formed without thermal degradation. In this paper, we investigate whether the new zone-heating procedure can induce the macroscopic orientation of the microdomains in the bulk of bcps having high values of N. If this is the case we shall present a possible model leading to macroscopic orientation of the lamellar microdomains.

2. Experimental method

2.1. Sample preparation

The characteristics of the SI dibcp (coded as SI-4) used in this study are listed in Table 1. This symmetric dibcp was prepared by a sequential living anionic polymerization with *sec*-butyllithium as an initiator and cyclohexane as a solvent. The dibcp SI-4 forms the lamella microdomain structure having the domain spacing (D_{lam}) of 62 nm in the thermodynamically stable state, where D_{lam} was determined by small angle X-ray scattering (SAXS) measurements.

The sample of SI-4 used in this work was mixed with a small amount of antioxidant (Irganox1010) (0.1 wt%), and cast into films from a homogeneous solution in cyclohexane with a total polymer concentration of 10 wt% at room temperature. It should be noted that cyclohexane is a good solvent for PI but a poor solvent for PS. Thus, the hex-cyl of PS block chains in the matrix of PI block chains is formed in the as-cast film rather than the equilibrium lamellar microdomain morphology. SAXS patterns from the as-cast film revealed that the cylinder axis of hex-cyl is preferentially oriented parallel to the film surface but has a rotational freedom around film normal **n** as shown in Fig. 2a [18]. The characterization of the microdomain structure will be discussed in Sections 3.1 and 3.2.

We applied the annealing at a constant temperature without the zone heating and the zone heating to the as-cast films in order to clarify how the zone heating affects the macroscopic orientation of hex-cyl. The annealing free from ∇T field was done in vacuum for 12 h at 120 °C which is above $T_{g,PS}$ but below T_{ODT} (at least above 200 °C judging from the phase diagram of hex-cyl of SI [19,20]), in order to achieve the transition from the nonequilibrium hex-cyl to the equilibrium lamella. The obtained film was quenched below T_g by quickly dunking it into liquid N_2 in order to solidify the structure developed by the annealing. In the cold zone-heating method, we employed a sharp effective temperature gradient of $|\nabla T|_{eff} = 13\ °C/mm$ ($8.2 \times 10^{-4}\ °C/D_{lam}$) with the high temperature $T_1 = 160$ °C and the low temperature $T_2 = 10$ °C across $T_{g,PS}$. The moving rate of ∇T was 25 nm/s (0.40 D_{lam}/s).

Since the hex-cyl in the as-cast film was already oriented preferentially with respect to the film surface, we need to consider the effects of the pre-orientation of hex-cyl on the macroscopic orientation attained after the zone heating. Thus, two kinds of the zone-heating experiments were conducted by changing the relationship between the direction of the moving ∇T axis and the orientation of the as-cast film surface with sheet 1 and sheet 2 which were prepared by stacking the as-cast films differently as shown in Fig. 2b. In the case of the sheet 1, **n** is parallel to the O*z* direction, so that the cylinder axis is preferentially oriented perpendicular to the direction of the moving ∇T. On the other hand, in the case of the sheet 2, **n** is perpendicular to the O*z* direction, so that the cylinder axis is not always perpendicular to the direction of the moving ∇T but is randomly rotated in the O*xz* plane as shown in parts b–d. Each of the sheets of 2 mm thickness and 10 mm width was placed inside the cell made of polytetrafluoroethylene (PTFE) [part (1) in Fig. 2c]. One side of the sheet contacted with a glass

Table 1
Characteristics of the sample used in this work

Code	M_n[a]	M_w/M_n[b]	f_{PS}[c]
SI-4	8.9×10^4	1.04	0.51

[a] M_n: number-average molecular weight estimated by gel permeation chromatography (GPC).
[b] M_w/M_n: polydispersity index where M_w is weight-average molecular weight measured by GPC.
[c] f_{PS}: volume fraction of polystyrene estimated by using M_n of each block in SI-4, and assuming densities of PS and PI in the system to be equal to those of corresponding homopolymers [31,32].

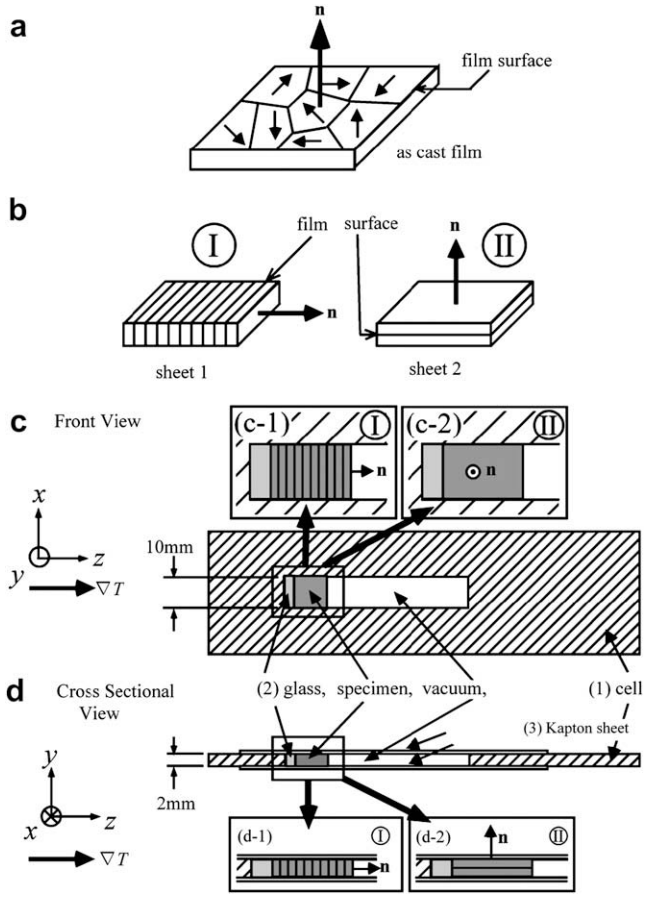

Fig. 2. Schematic illustrations of the as-cast film (a), the sheets 1 and 2 (b) prepared from the as-cast films, and the sample cell used for the zone-heating device (c and d). (a) Cylinder axes tend to be preferentially oriented perpendicular to the normal vector **n** of the as-cast film surface. The directions of cylinder axes are indicated by the arrows. (b) In the sheet 1, the film specimens were stacked in the sample cell with **n** parallel to the ∇T axis, while, in the sheet 2, the film specimens were stacked with **n** perpendicular to the ∇T axis. (c) A top view and (d) a cross-sectional view of the sample cell through its center line. Each specimen of the sheets 1 and 2 was placed inside the cell made out of polytetrafluoroethylene (PTFE) [part (1)] with a glass surface [part (2)]. Thin polyimide sheets (Kapton®) [part (3)] were placed on both sides of the PTFE cell normal to O*y* axis.

(soda-lime glass) [part (2)], and the top and bottom parts of the sample sheet parallel to the O*xz* plane contacted with the polyimide (Kapton®) sheets [part (3)] as shown in Fig. 2d. The ∇T axis and its moving direction were set along the O*z* direction, and the glass surface contacted with the sheets in the O*xy* plane. After the application of the zone heating, the two zone-heated sheets 1 and 2 were quenched below T_g by quickly dunking it into liquid N_2 in order to solidify the structure developed via the zone-heating method.

2.2. Small angle X-ray scattering (SAXS)

SAXS measurements were conducted at room temperature on the as-cast film, the annealed film, and the two kinds of zone-heated sheets 1 and 2. For this purpose, we cut a specimen out from each of the solidified zone-heated sheets into a rectangular parallelepiped shape as shown in Fig. 3. The specimens had dimensions along the O*x*, O*y*, and O*z* direction as given by $-1.0 \le x/\mathrm{mm} \le 1.0$, $-1.0 \le y/\mathrm{mm} \le 1.0$, $0 \le z/\mathrm{mm} \le 2.0$. Here, we set the origin of the Cartesian coordinate at the center of the glass surface. The SAXS measurements were conducted by using the synchrotron radiation small angle X-ray scattering apparatus, as detailed elsewhere [21],

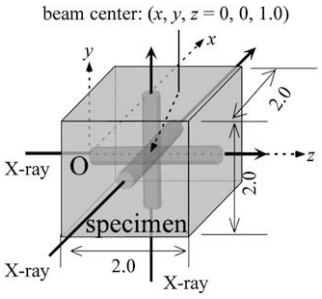

Fig. 3. Schematic diagram indicating geometric relationships among the three directions of the incident X-ray beam, the zone-heated specimen, and the Cartesian coordinate. The incident X-ray beams were irradiated from three orthogonal directions along the *x*, *y*, and *z* directions through a common center of (0, 0, 1.0). The numbers are expressed in unit of mm.

at the beamline 15A of the Photon Factory, Institute of Materials Structure Science, High Energy Accelerator Research Organization, Tsukuba, Japan. The wavelength (λ) of incident X-ray was 0.15 nm and the spectral distribution $\Delta\lambda/\lambda$ was 10^{-3}. The sample-to-detector distance was 2.3 m and the beam size at the sample surface was 0.5×0.5 mm. Two-dimensional (2D) SAXS patterns were obtained with a stage-mounted imaging plate (IP) system [22]. In the case of the experiments conducted on the as-cast film and the annealed film, the incident beam was irradiated from the direction parallel (through view) and perpendicular (edge view) to **n**, and thicknesses of specimens along incident beam in both views were set 2 mm. In the case of the experiments conducted on the zone-heated specimen, the incident beam was irradiated from three orthogonal directions, along the O*x*, O*y*, and O*z* directions, through a common center of (0, 0, 1.0) (Fig. 3) in order to investigate the orientation of lamellae developed via the zone-heating process. The exposure time was 1 s to obtain each two-dimensional (2D) SAXS pattern.

2.3. Transmission electron microscopy (TEM)

Transmission electron microscopy (TEM) was conducted on the as-cast film by using JEOL JEM-2000FXZ transmission electron microscope operated at 120 kV in order to investigate the morphology of microdomains in the as-cast film. The as-cast film was microtomed into ultrathin sections of *ca.* 50 nm thickness at -90 °C with a Reichert-Nissei ULTRACUT N® together with a cryogenic unit FC 4E and glass knives which were set parallel to the film surface and moved perpendicular to **n**. The ultrathin sections were picked up on 400 mesh copper grids and stained by the vapor of 2% O_sO_4 (aq) for 1 h at room temperature. Therefore, PS and PI domains are observed as bright and dark in the TEM images, respectively.

3. Results

3.1. Hex-cyl in as-cast film

2D-SAXS patterns for the as-cast film are shown in Fig. 4a and b, where the incident X-ray beam irradiated parallel and perpendicular to **n** (the through and edge views, respectively). The circular averaged intensity of the through view pattern (Fig. 4a) with respect to q is plotted as a function of q in the bottom of Fig. 4c, where q is the magnitude of scattering vector (**q**). The intensities along $\mu = 0°$ and 90° direction in the edge view pattern (Fig. 4b) are plotted as a function of q in the top and middle of Fig. 4c, respectively. Here, μ is the azimuthal angle defined in Fig. 4b. The observed peaks are located at q_m, $\sqrt{3}q_m$, $\sqrt{4}q_m$, $\sqrt{7}q_m$, and $\sqrt{9}q_m$ in the top profile in Fig. 4c, and q_m, $\sqrt{3}q_m$, $\sqrt{4}q_m$ in the middle and bottom profile in Fig. 4c, where q_m is q value at the 1st order

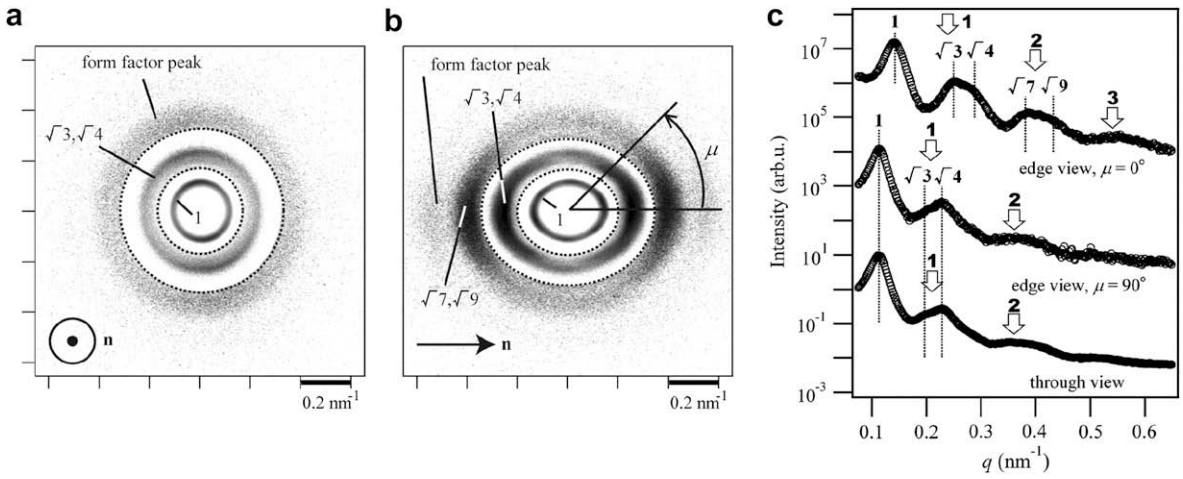

Fig. 4. 2D-SAXS patterns obtained for the as-cast film by irradiating the incident X-ray beams along the direction parallel (a, through view) and perpendicular (b, edge view) to the film normal **n**. The intensity inside the smaller dotted circle was multiplied by 0.04 times, while the intensity outside the larger dotted circle was multiplied by 6 times. The circularly averaged intensities of the through view pattern in part (a) are plotted as a function of q (bottom curve of c). The intensities along $\mu = 90°$ and 0° in the edge view pattern in part (b) are plotted as a function of q (middle and top curve of c, respectively). In part (c), the intensity data of the bottom curve are actual values, and the other data were shifted up vertically by 3 order of magnitudes relative to the intensities immediately below in order to avoid an overlap of the curves.

maximum intensity. These peak ratios indicate that the bcp formed hex-cyl in the as-cast film. In the TEM image in Fig. 5, the bright circles on the hexagonal lattice and the bright and dark stripes reveal the two grains of hex-cyl with different orientations, supporting that hex-cyl was formed in the as-cast films.

The orientation of hex-cyl in the as-cast film can be also clarified on the basis of the SAXS data shown in Fig. 4. In the edge view (Fig. 4b), the 2D-SAXS pattern has an anisotropy in the scattering intensity distribution with respect to μ, which can be quantitatively displayed in Fig. 4c. The top profile obtained at $\mu = 0°$ in Fig. 4c tends to exhibit the higher order peaks more clearly than the middle profile obtained at $\mu = 90°$, and the maximum intensity of the former is larger than that of the latter by the factor of 1.3 times. These results indicate that lattice planes of hex-cyl and hence the cylinder axes tend to orient perpendicular to **n**. On the other hand, in the through view (Fig. 4a), the 2D-SAXS pattern is isotropic, indicating that the cylinder axis has uniform rotational freedom with respect to **n**. Thus, the above-mentioned orientation of hex-cyl is consistent with that mentioned in Section 2.1 and shown in Fig. 2a.

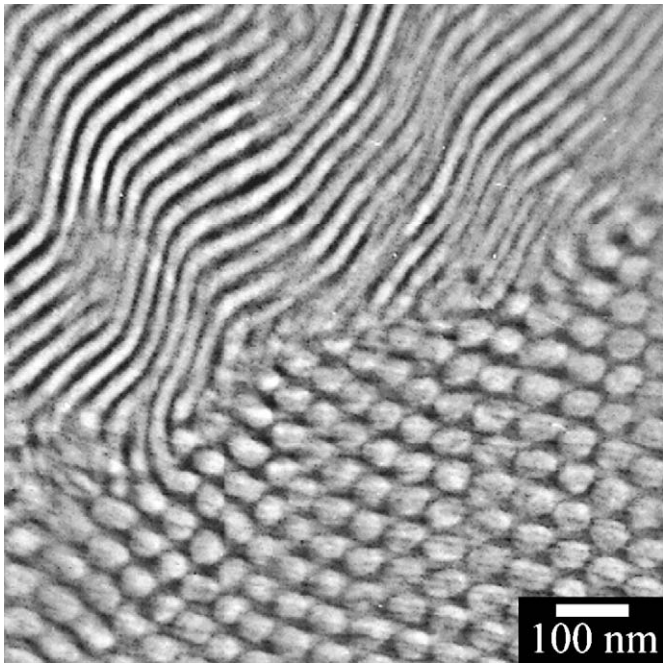

Fig. 5. TEM image obtained for the as-cast film.

The ellipsoidal shape of the scattering pattern in Fig. 4b reflects that there are deformations of the lattice of hex-cyl and the cylinder itself. The deformation of lattice can be evaluated by comparing $D_\perp$ with $D_\parallel$, where $D_\perp$ and $D_\parallel$ are Bragg spacings of (100) plane along the direction perpendicular and parallel to the film normal **n**, respectively. $D_\parallel$ and $D_\perp$ are calculated with $D_i = 2\pi/q_{m,i}$ ($i = \perp$ or $\parallel$) with respect to the top ($\mu = 0°$) and middle ($\mu = 90°$) profile in Fig. 4c, respectively. Here, $q_{m,\perp}$ and $q_{m,\parallel}$ are q_m of the middle and top profile, respectively. The deformation of the cylinder itself can be evaluated by comparing $r_\perp$ with $r_\parallel$, where $r_\perp$ and $r_\parallel$ are the radii of cylinders along the direction perpendicular and parallel to the film normal **n**, respectively. $r_\perp$ and $r_\parallel$ were estimated from the form factor peaks originating from cylinder structures (open thick arrows in Fig. 4c). The cylinder structures exhibit the form factor peaks which satisfy

$$q_j r = 4.98, 8.364, 11.46, \ldots \quad \text{for } j = 1, 2, 3, \ldots \tag{1}$$

where q_j is the q value at the jth-order form factor peak and r is the radius of cylinders [23]. The peaks indicated by open thick arrows in Fig. 4c satisfy Eq. (1), so that we can evaluate r_i [24]. The evaluated r_i is summarized together with D_i in Table 2, where $D_\perp$ is larger than $D_\parallel$, and $r_\perp$ is larger than $r_\parallel$, consistent with the previous report [17].

The results of calculations of D_i and r_i indicate that the hexagonal lattice and the cylinder are compressed along the direction parallel to **n**. This compression reflects one-dimensional contraction of the swollen hex-cyl along **n** during the solvent evaporation

Table 2
Characterization of the hex-cyl in the as-cast films by SAXS[a]

$D_\perp$	$D_\parallel$	$r_\perp$	$r_\parallel$
55	44	23	21

$D_\perp$ and $D_\parallel$: the Bragg spacing of the (100) plane of the distorted hex-cyl along the direction perpendicular and parallel to the film normal **n**, respectively.
$r_\perp$ and $r_\parallel$: the radius of the distorted cylinder along the direction perpendicular and parallel to the film normal **n**, respectively.
[a] All the values indicated are in unit of nm.

process. When an effective repulsive interaction of each block chain becomes large enough during the solvent evaporation process, hex-cyl of PS block chains is formed in the matrix of PI block chains, where both the PS cylinders and the PI matrix are still swollen with the solvent. The successive evaporation of solvent brings about a volume contraction. In the contraction, the thickness of the cast solution decreases, while the area of its surface is kept constant, resulting in one-dimensional contraction of the system along **n**. This one-dimensional contraction leads to anisotropic contraction of the radius of cylinders and the lattice spacing of hex-cyl, resulting in the cylinders having elliptical cross-sections with their long axes oriented parallel to the film surface and the lattice of hex-cyl being compressed along the direction parallel to **n**.

3.2. Lamellae developed upon annealing without applied field

Fig. 6a and b shows 2D-SAXS patterns from the through and edge views of the annealed film at 120 °C for 12 h, respectively. Both patterns are independent of μ. Thus, we plotted the circularly averaged intensity data as a function of q in Fig. 7a. In both plots for the edge and through view, there are peaks at q_m, $3q_m$, and $5q_m$. These ratios of the scattering peak position indicate that the bcp forms the lamella with the spacing $D_{lam} = 62$ nm in the annealed film. The scattering maxima at $2q_m$ and $3q_m$ are suppressed, because the volume fraction of PS is almost identical with that of PI [25,26]. As shown in Fig. 7b and c, the intensities at $3q_m$ in the through and edge views are almost independent of μ. Thus, the bcp forms the lamellae with a random orientation in the annealed film.

3.3. Lamellae developed in zone-heated sheets

The 2D-SAXS patterns obtained for the zone-heated sheet 1 with $\mathbf{n} \parallel \nabla T$ are shown in Fig. 8. Fig. 8a–c shows the 2D-SAXS patterns observed in the q_yq_z, q_xq_z, and q_xq_y planes, respectively. Here q_x, q_y, and q_z are x, y, and z components of scattering vector **q**, respectively. All scattering patterns have peaks at $q/q_m = 1, 2, 3, 4, 5\ldots$, indicating that the nonequilibrium hex-cyl transformed into the equilibrium lamella by the zone heating. In Fig. 8a and b, each scattering maximum at q_m, $2q_m$, $3q_m$, $4q_m$, and $5q_m$ exists in the direction parallel to the ∇T direction. On the other hand, in Fig. 8c, all scattering maximums are weaker than those in Fig. 8a and b by a factor of about 0.4, and there is almost no μ-dependence in the scattering peaks. These results indicate that, in the zone-heated sheet 1, the bcp forms the lamellae with their interfaces preferentially aligned perpendicular to the ∇T direction and to the sheet surfaces (parallel to the xz plane). The macroscopic orientation of lamellae is visualized schematically on the top of Fig. 8a–c.

The 2D-SAXS patterns obtained for the zone-heated sheet 2 with $\mathbf{n} \perp \nabla T$ are shown in Fig. 9. Fig. 9a–c is that observed in the q_yq_z, q_xq_z, and q_xq_y planes, respectively. The features of the patterns are essentially similar to those of the patterns in Fig. 8. In Fig. 9a and b, each scattering maximum at q_m, $2q_m$, $3q_m$, $4q_m$, and $5q_m$ exists in the direction parallel to ∇T direction as found for the sheet 1 shown in Fig. 8a and b. However, they do not exhibit the μ-dependence as sharp as those in Fig. 8a and b, indicating that an orientation distribution of the lamellar normals ($\mathbf{n}_l$) with respect to the ∇T axis is broader in the sheet 2 than in the sheet 1. In Fig. 9c, all the scattering maxima are much weaker than those in Fig. 9a and b, and there exhibit almost no μ-dependence. These results indicate that, in the zone-heated sheet 2 also, the bcp forms the lamellae having essentially the same orientation as in the zone-heated sheet 1. The macroscopic orientation is schematically visualized again on the top of Fig. 9a–c.

4. Discussion

4.1. Lamellae developed upon annealing without applied field

In this section, we shall discuss the OOT process from the nonequilibrium hex-cyl in the as-cast film to the equilibrium lamella in the annealed film. According to our SAXS measurements described in Sections 2.1 and 3.1, the spacings of (100) plane of the hex-cyl ($D_\perp$ and $D_\parallel$) are closer to D_{lam} than those of the other lattice planes of the hex-cyl. This result indicates that (100) planes of the hex-cyl transform into lamella plane of the equilibrium lamella, as elucidated previously [17].

This OOT process can be explained by the model proposed by Hashimoto, Sakurai, and coworkers [17]. We shall briefly review the model, because the model is crucial to explain the macroscopic orientation of lamellae created by imposing the zone heating during the OOT process. The model involves the coalescence of two neighboring cylinders as shown in Fig. 10a. Fig. 10a-1 represents the hex-cyl in the as-cast film, where the PS and PI block chains have unfavorable chain conformations in the bulk which is brought about by vitrification of the PS cylinders during the solution casting process and by a further evaporation of solvents into a bulk specimen. The relaxation of the unfavorable chain conformations occurs in the as-cast sheet upon annealing above

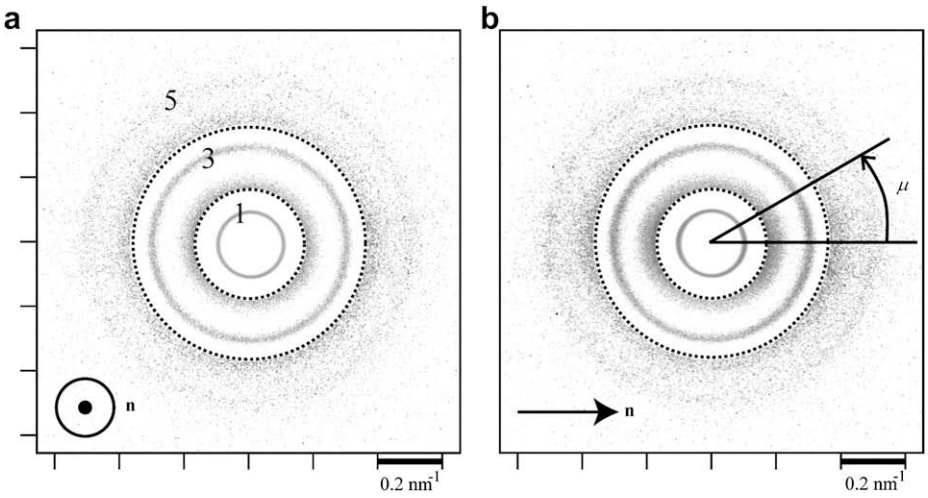

Fig. 6. 2D-SAXS patterns obtained for the annealed film at 120 °C without an application of the zone heating by irradiating X-rays along the direction parallel (a, through view) and perpendicular (b, edge view) to **n**. The circular dotted lines have the same meaning as those in Fig. 4.

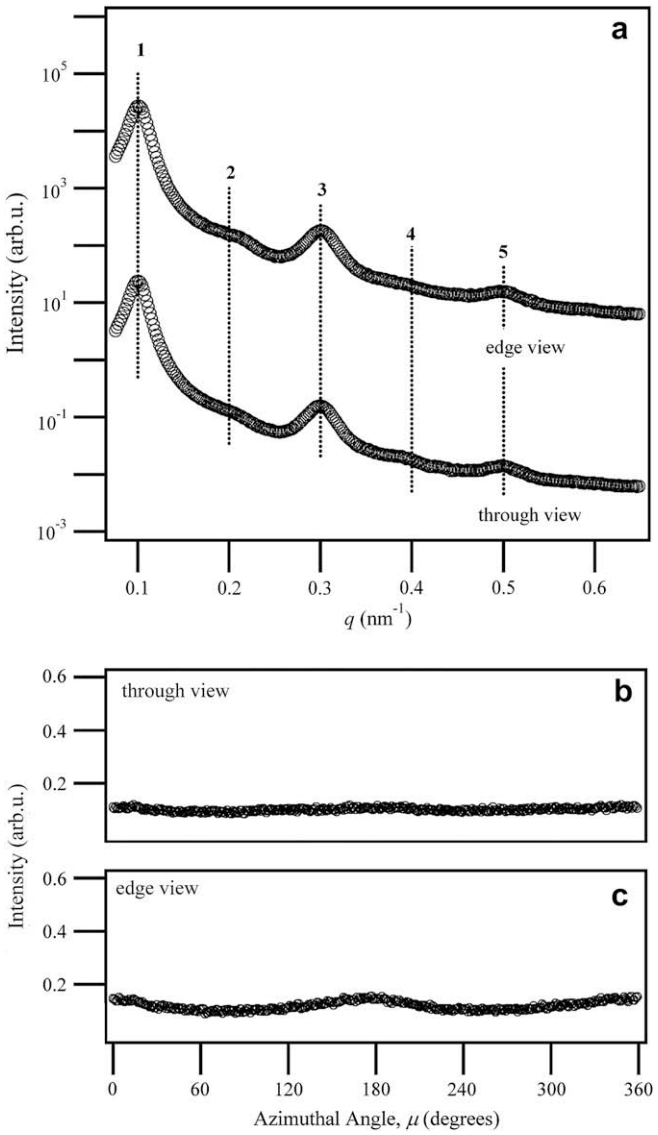

Fig. 7. The circularly averaged intensities of the 2D-SAXS in Fig. 6a and b are plotted as a function of q in the bottom and top of part (a), respectively. Parts (b) and (c) show μ-dependence of the intensity at $3q_m$ in the 2D-SAXS patterns in Fig. 6a and b, respectively. In part (a), the intensity data of the bottom curve are actual values, and the data of the top curve were shifted up vertically by 3 order of magnitudes relative to the intensity data of the bottom curve in order to avoid an overlap of the curves.

$T_{g,PS}$, resulting in a change in the interface curvature of cylinders so as to reduce their mean curvature, which may bring about a change of the cross-sectional shape of cylinders being more elliptical and an undulation of the flattened cylinders as shown in Fig. 10a-2. When the undulating interfaces approach each other and coalesce, channels connecting between the neighboring cylinders can be formed as shown in Fig. 10a-3. The channels grow along the direction of the cylinder axis in such a way that the cylinders are eventually transformed into lamellae which are thermodynamically stable at the annealing temperature (Fig. 10a-4). This coalescence of cylinders driven by the interface curvature change should occur along the (100) plane of hex-cyl, because the distance between two neighboring cylinders becomes minimum in the (100) plane.

Fig. 10b schematically illustrates formation of the lamellae having three different orientations (shown in b-3) from the given single grains of hex-cyl shown in (b-1) upon the annealing above $T_{g,PS}$. In the early stage of the annealing, the distorted hex-cyl is expected to be transformed into regular hex-cyl as shown in Fig. 10b-1, In the regular hex-cyl, there are three possible directions of (100) planes along which the cylinders are transformed into lamellae (Fig. 10b-2). The annealing without applied fields will not select any particular directions for the transformation. Thus, the perfectly aligned cylinders create the three orientations of lamellae, and hence the OOT without the external field increases the initial orientation distribution of hex-cyl as shown in Fig. 10b-3.

4.2. OOT under zone heating

4.2.1. Estimation of lamellar orientation

We shall explore the orientation of lamellae attained by the zone-heating-induced OOT. In order to clearly show the orientation of the zone-heated sheet 1, we plotted μ-dependence of the scattering intensity at $3q_m$ in the q_yq_z, q_xq_z, and q_xq_y planes as shown in Fig. 11a–c, respectively. We also plotted those for the zone-heated sheet 2 as shown in Fig. 11d–f, respectively.

In the case of the zone-heated sheet 1, the lamellar interfaces preferentially align perpendicular to the ∇T direction, as indicated by two peaks at $\mu = 0°$ and 180° in Fig. 11a and b. The SAXS patterns in the q_yq_z and q_xq_z planes are essentially the same, while the SAXS pattern in the q_xq_y plane has the weak scattering intensity almost independent of μ, indicating that the distribution of the direction of $\mathbf{n}_l$ has a uniaxial symmetry with respect to the ∇T direction. Moreover the distribution is sharp around the ∇T axis.

In the case of the zone-heated sheet 2 also, the lamellar interfaces preferentially align perpendicular to the ∇T direction, and the distribution of the direction of $\mathbf{n}_l$ has a uniaxial symmetry with respect to the ∇T direction, as is evidenced by Fig. 11d–f. However, the alignment of $\mathbf{n}_l$ along the ∇T direction for the zone-heated sheet 1 is much sharper than that for the zone-heated sheet 2, as evidenced by the sharper μ-dependence of the intensity maximum in the sheet 1 than in the sheet 2. The half-width at half maximum (σ) of the peak at $\mu = 180°$ in the q_yq_z and q_xq_z planes were measured to be $\sigma = 29°$ (Fig. 11a) and 22° (Fig. 11b) for the zone-heated sheet 1, while $\sigma = 42°$ (Fig. 11d) and 47° (Fig. 11e) were obtained for the zone-heated sheet 2. This result indicates that the distribution of the direction of $\mathbf{n}_l$ in the zone-heated sheet 1 is narrower than that in the zone-heated sheet 2.

Under the uniaxial orientation distribution of $\mathbf{n}_l$ with respect to the ∇T axis, we can evaluate the orientation factor (f) of $\mathbf{n}_l$ with respect to ∇T axis by

$$f = \frac{3\langle \cos^2 \alpha \rangle - 1}{2} \tag{2}$$

where α is the angle between $\mathbf{n}_l$ and the ∇T direction. It should be noted that $f = 1$ for a perfect orientation and 0 for a random orientation. In Eq. (2) $\langle \cos^2 \alpha \rangle$ is given by

$$\left\langle \cos^2 \alpha \right\rangle = \frac{\int_0^{\pi/2} (\cos^2 \mu) I(\mu) \sin \mu \, d\mu}{\int_0^{\pi/2} I(\mu) \sin \mu \, d\mu} \tag{3}$$

where $I(\mu)$ is the azimuthal angle dependence of scattering intensity at $3q_m$. Calculated fs are 0.30 and 0.16 for the zone-heated sheets 1 and 2, respectively, indicating that the value f is larger in the zone-heated sheet 1 than that in the zone-heated sheet 2. This difference in the distribution between two sheets is due to the difference in the relationship between the ∇T direction and the orientation of the hex-cyl in the sheets before the zone heating as will be detailed in Section 4.2.4 later. It is noted that the degree of orientation of the lamellae attained with this method is far less than that through the hot zone-heating involving ODT where $f = 0.93$ [2,3,27].

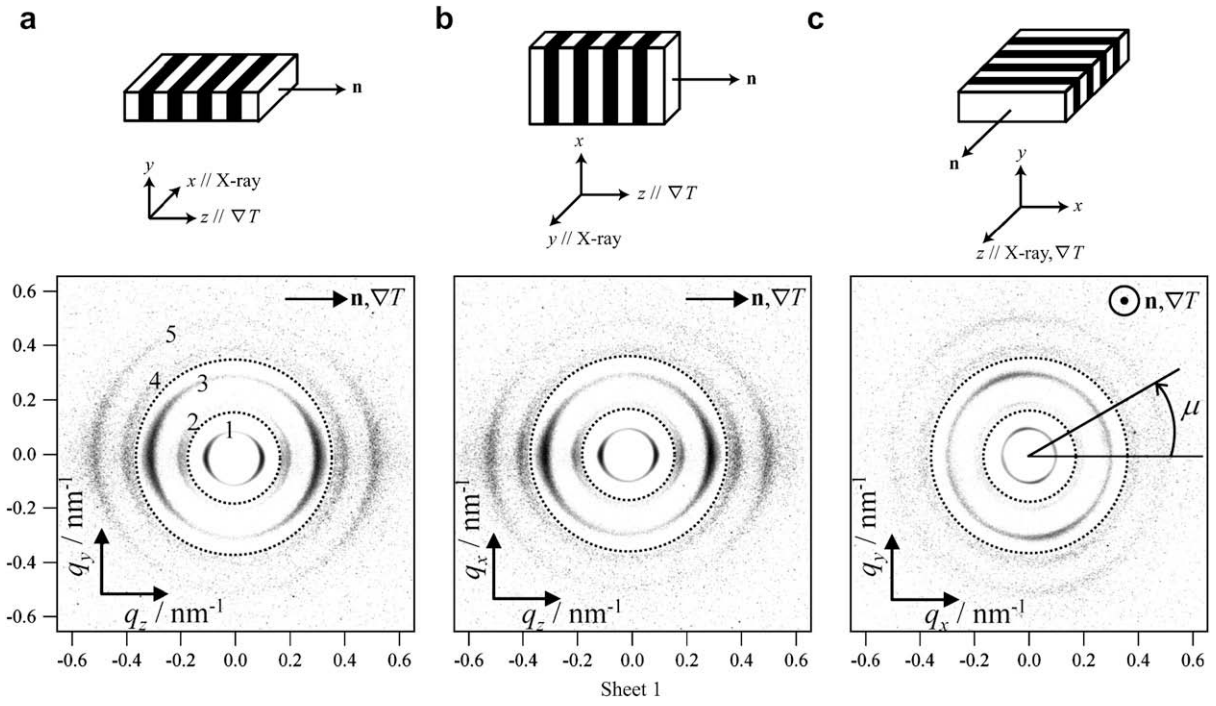

Fig. 8. 2D-SAXS patterns obtained for the zone-heated sheet 1 by irradiating X-rays along O*x*, O*y*, and O*z* directions through a common center (*x*/mm, *y*/mm, *z*/mm = 0, 0, 1.0) (a, b, and c, respectively). Schematic illustrations indicating the orientation of lamellae obtained by the zone heating are shown on the top of each 2D-SAXS pattern.

4.2.2. Mechanism of lamellar orientation through the zone-heating-induced OOT: thermodynamic interpretation

Let us now discuss a possible scenario for the lamellar orientation attained through the zone-heating-induced OOT from the thermodynamic viewpoint. As a first step, we consider the simplest possible case where (i) the hex-cyl in the as-cast film has a special orientation as specified in Fig. 12a and (ii) the moving rate of the ∇*T* field is slow enough compared to the rate of OOT, so that the transformation from hex-cyl to lamella occurs, in the narrow slit-like region parallel to the glass surface, sequentially from the region near the glass surface toward the region in the interior of the specimen (see Section 1). As shown in Fig. 12a, in the narrow

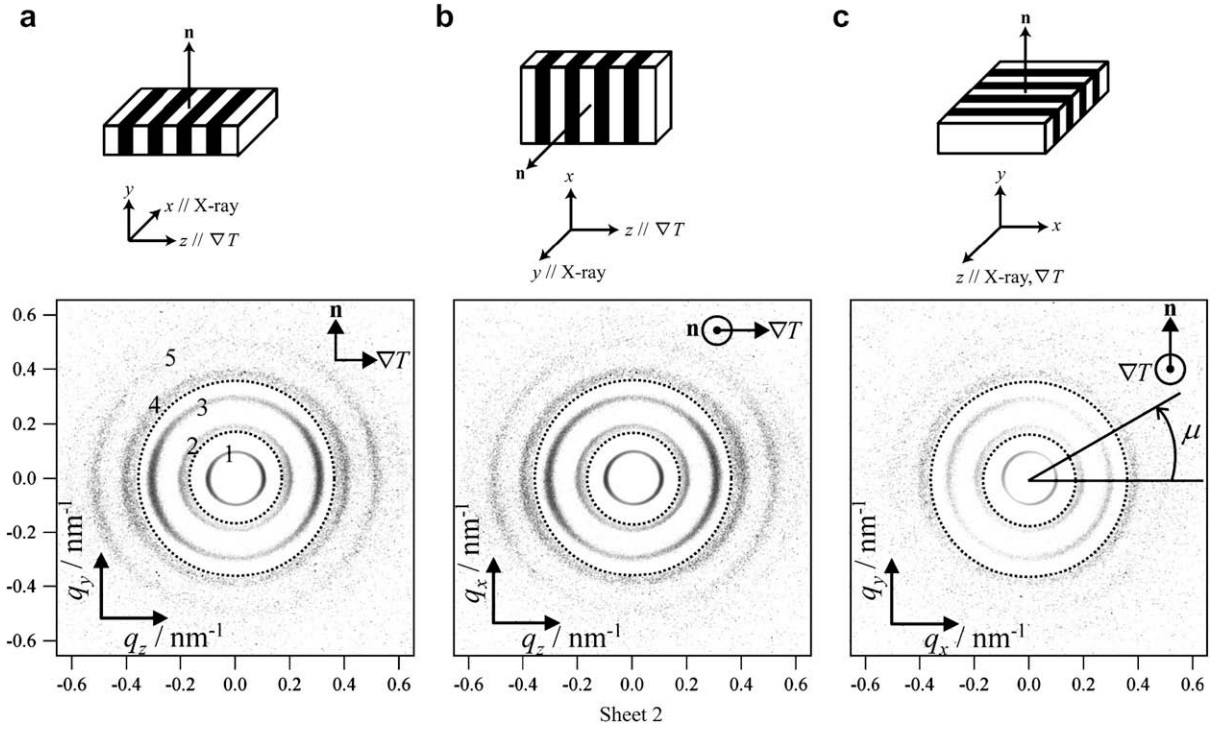

Fig. 9. 2D-SAXS patterns obtained for the zone-heated sheet 2 by irradiating X-rays along O*x*, O*y*, and O*z* directions through a common center (*x*/mm, *y*/mm, *z*/mm = 0, 0, 1.0) (a, b, and c, respectively). Schematic illustrations indicating the orientation of lamellae obtained by the zone heating are shown on the top of each 2D-SAXS pattern.

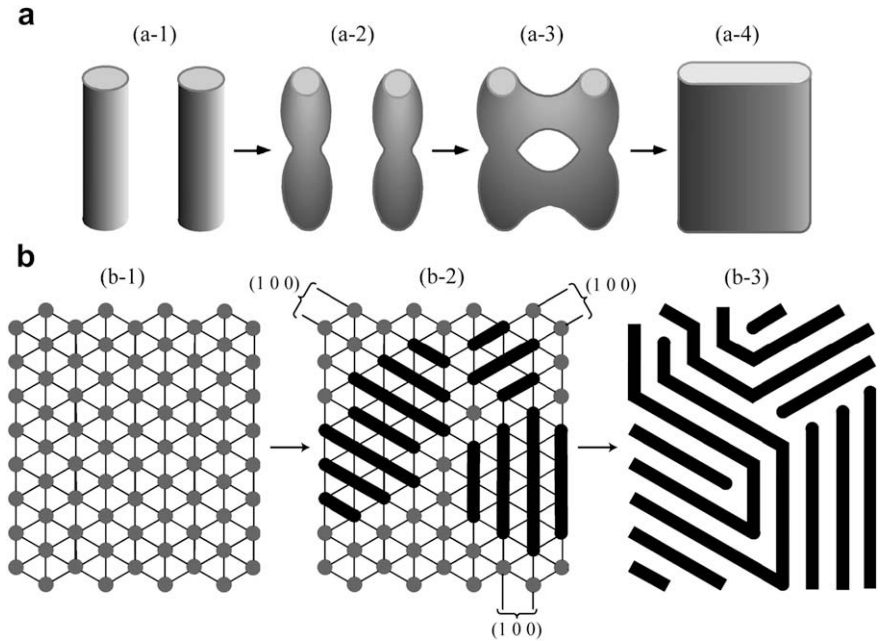

Fig. 10. (a) Schematic illustration for the OOT process from hex-cyl to lamellae which involves deformation and coalescence of two cylinders along the (100) plane of hex-cyl. (b) The OOT process in the case of the annealing without the ∇T field, which is viewed from the direction along the cylinder axis. There are three equivalent (100) lattice planes in the hex-cyl (part b-2), so that the resulting lamellae have the three specific orientations (part b-3).

slit-like region near the glass surface there are essentially three directions, A, B, and B′ (counter part of B which is not shown in part a) along which the cylinders are transformed into lamellae. The transformation will develop the lamellar orientation with their interfaces parallel to the glass surface as shown in Fig. 12b or the lamellar orientation with their interfaces inclined to the glass surface by $+60^\circ$ as shown in Fig. 12c. Note that the counter plane of B (B′) will encounter by the same effect as B.

This OOT process in the slit-like region occurs under the influence of the external field given by the glass surface through the packing of the PI block chains, which emanate from the lamellar interface close to the glass surface, in the narrow space between the glass surface and the lamellar interface under the demand of the incompressibility, as shown in the inset to Fig. 12b and c. Since the interfacial tension between PS and glass is smaller than that between PI and glass [4], it is unfavorable that PI block chains emanating from the PS domain in the sheets 1 and 2 directly contact with the glass surface. In order to avoid this situation, a part of the bcps is considered to form a monolayer on the glass surface as schematically shown in Fig. 12a–c during the OOT induced by the zone-heating process. In this monolayer, the layer on the glass side is occupied by the PS block chains, while the layer on the interior side of the specimen is occupied by the PI block chains, so that PI block chains emanating from the PS cylinder or lamella contact with the PI monolayer on the glass surface.

As illustrated in the inset to Fig. 12b and c, the packing of the chains near the glass surface favors the lamellar orientation (b) rather than the lamellar orientation (c), simply because the

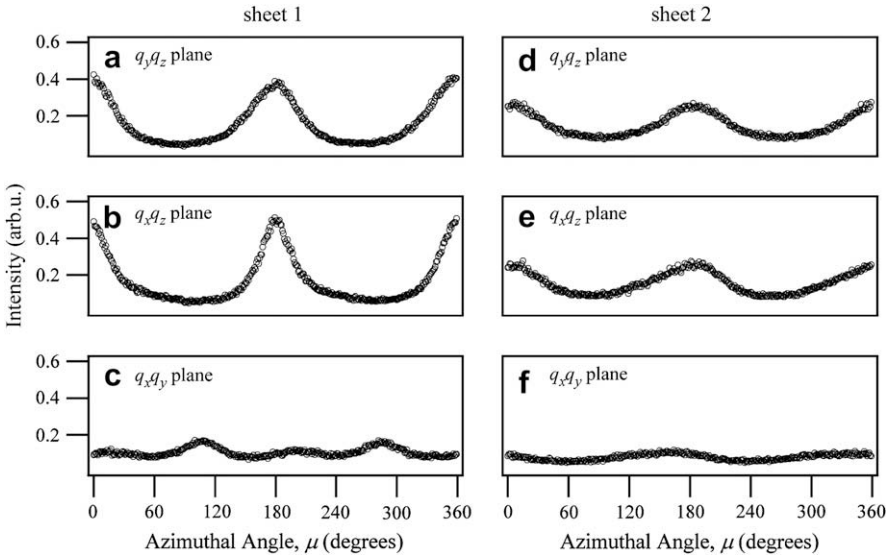

Fig. 11. Parts (a–c) and (d–f) show μ-dependence of the intensity at $3q_m$ in the 2D-SAXS patterns in Fig. 8a–c (zone-heated sheet 1) and Fig. 9a–c (zone-heated sheet 2), respectively.

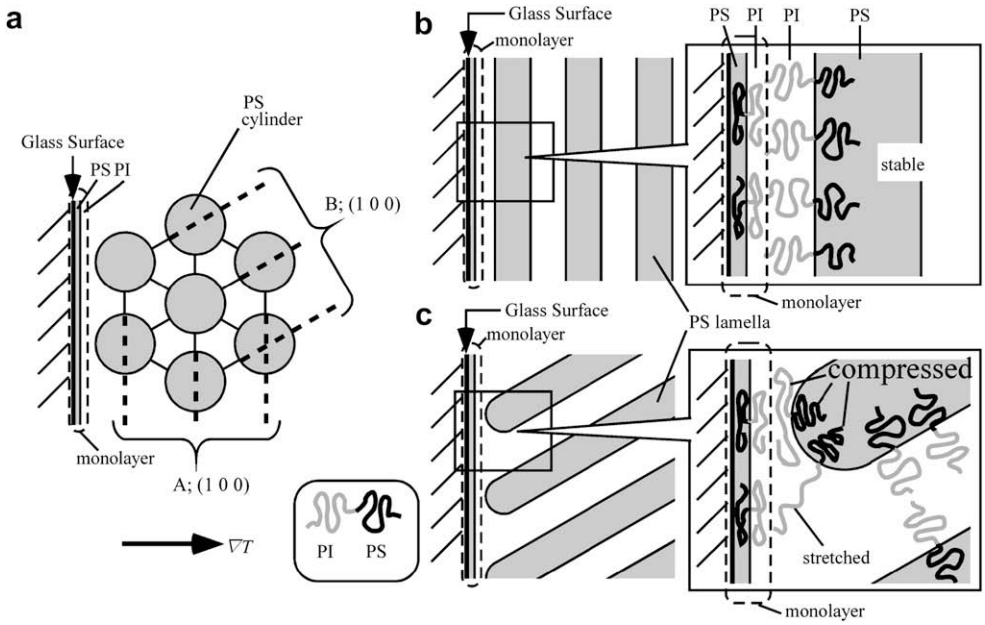

Fig. 12. Schematic illustration indicating the geometric relationship between the hex-cyl and the glass surface (a). There are three kinds of the (100) planes of hex-cyl; one is parallel to the surface (A), another is inclined with respect to the surface by the angle of 60° (B), and the counter part of B (B′ having the angle −60° with respect to the surface) is not shown in the figure. The (100) plane A transforms to the lamella parallel to the surface (b), and the (100) plane B transforms to the lamella inclined with respect to the surface by 60° (c). The conformational entropy loss of the block chains near the glass surface is smaller for the lamellar orientation (b) than for the lamellar orientation (c) as illustrated schematically in the inset to parts (b) and (c).

lamellar orientation (c) involves an extra stretching or compression of the block chains emanating from the interface of the lamellae near the glass surface and hence is subjected to a greater cost of the elastic free energy, compared with the lamellar orientation (b). Thus the lamellar orientation (b) is selected by the cold zone-heating process near the glass surface. When the ∇T front is moved toward the interior of the specimen along the z-axis, the OOT occurs in the new slit-like hot region above $T_{g,PS}$ under the external field given by the surface of the lamellae having the selected orientation (b). This moving ∇T field gives rise to the sequential transformation of hex-cyl into the lamella with its normal parallel to ∇T axis.

If there is orientation distribution of hex-cyl grains, in each grain one of the three (100) planes of hex-cyl with their normal vector closest to the ∇T axis will be selected for the transformation into lamellae. Hence the sequential OOT induced by the cold-zone heating will produce the preferential orientation of lamellar normals with respect to the ∇T axis.

4.2.3. *Mechanism of lamellar orientation through the zone-heating-induced OOT: kinetic interpretation*

Here again we consider first the simplest case as shown in Fig. 12a, and we try to give a possible kinetic interpretation on the preferential lamellar orientation. The hex-cyl in the as-cast film has a perfect orientation with respect to the moving front of ∇T as shown in Fig. 13b-1, where cylinders are shown by the dots and the moving ∇T front is shown by the dashed line. The left hand side of the front has $T > T_{g,PS}$ so that the OOT occurs, while the right-hand side of the front has $T < T_{g,PS}$ so that hex-cyl is trapped in a nonequilibrium state. We consider the case where the moving rate R of the front is sufficiently slow and comparable to the growth rate of the lamellar grains created through the OOT: hence the moving front does not leave a wide region of the bcp melt where the lamellar grains A and B (shown in Fig. 13b-1) for example grow equally well through the OOT via random nucleation and growth essentially free from the applied ∇T field.

In addition to the special conditions described above, we assume the grain of lamellae grows anisotropically through the OOT as elucidated earlier in the case of the lamellar growth from the disordered state [28–30], as illustrated in Fig. 13a: the growth rate of the grain along lamellar normal (v_{90}) is larger than that along the lamellar interfaces (v_0) so that the lamellar grain grown through the OOT has a prolate ellipsoidal shape. The growth of lamellar grain via OOT involves (i) a cooperative deformation of the cylinder interface which appears to propagate perpendicular to the (100) plane of hex-cyl with the rate v_{90} as well as (ii) coalescence of the deformed cylindrical interfaces and rearrangements of the chemical junctions of SI block chains toward lamellar interface which occur parallel to the interface with the rate v_0. Here it may be reasonable to assume that $v_{90} > v_0$, as supported by the experiments [28–30].

In order to simplify the discussion concerning the difference in the growth rate of the grains along the ∇T direction, we compare the growth rate of the lamellar grains A and B in part (b-1) where A and B have, respectively, the lamellar normal vector $\mathbf{n}_l$ parallel to ∇T direction and inclined to the ∇T direction by $-60°$. The growth rate of the grains A and B along the ∇T direction is v_{90} and v' ($=v_{90}\cos 60° = v_{90}/2$), respectively, where v_{90} is larger than v' by a factor of 2. If $v_{90} > R > v'$, the growth of the grain A can keep up with the shift of the moving ∇T front but the growth of the grain B cannot. If this is the case, during the ∇T front plane moves to the right-hand side, the grains A and B grow as shown in Fig. 13b-2. A further growth of the grain B may be hindered by the grain A as well by the nucleation and growth of the lamellar grain C from hex-cyl, for example, in which $\mathbf{n}_l$ is parallel to ∇T direction. Although another nucleation and growth giving rise to the grain B′ (the counter part of the grain B) in which $\mathbf{n}_l$ is inclined to the ∇T direction by $+60°$ may occur, the growth of the grain B′ along the ∇T direction is hindered by the growth of the grain A in the same way as the growth of the grain B. Thus, in the case where $v' < R < v_{90}$, the resulting texture is preferentially occupied by the grains in which $\mathbf{n}_l$ is parallel to ∇T direction as shown in Fig. 13b-3. In the case where $v_{90} > v' > R$, both the grains B (or B′) and A can keep up with the shift of the moving ∇T front, but the grain A grows faster than the grain B (or B′), thus resulting in the preferential orientation $\mathbf{n}_l$ along the ∇T axis. Thus $R < v_{90}$ provides the

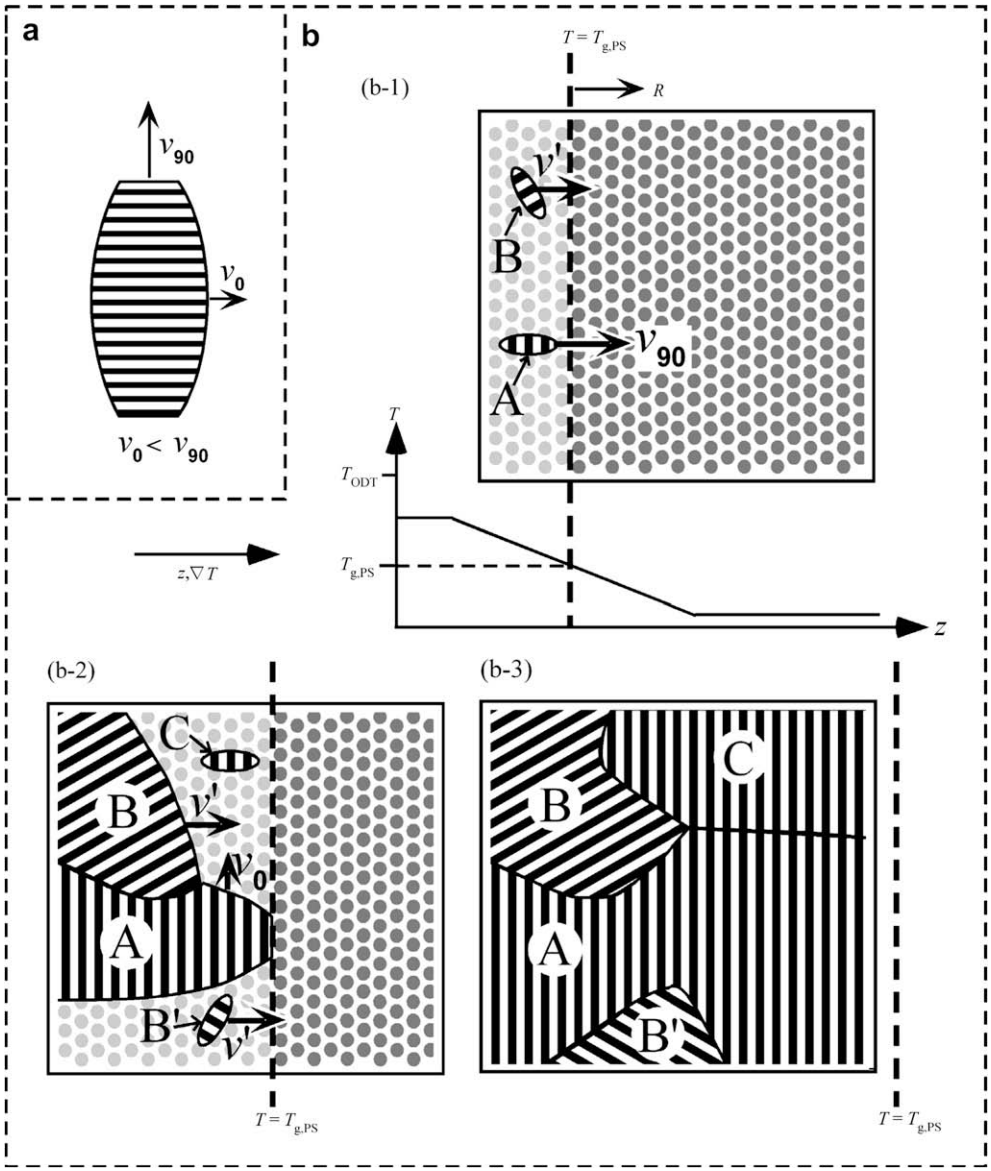

Fig. 13. (a) Schematic illustration for anisotropic growth of the lamella grain through the OOT from hex-cyl to lamella: the growth rate of the grain parallel to the lamellar normal $\mathbf{n}_l$ (v_{90}) is assumed to be larger than that perpendicular to $\mathbf{n}_l$ (v_0). (b) Schematic illustration indicating the selective growth of the lamellar grains having $\mathbf{n}_l$ parallel to the ∇T direction under the cold zone-heating process. The grains A and C which have a largest growth rate along the ∇T direction become dominant over other grains during the zone-heating process involving OOT. The illustration assumes a particular orientation of hex-cyl with respect to the moving front of the ∇T field.

necessary and sufficient condition for the preferential orientation of $\mathbf{n}_l$ along the ∇T axis. Although v_{90} was not yet experimentally evaluated, the assumption of $R < v_{90}$ seems to be satisfied in the light of our experimental results. The measurements of the growth rates v_0 and v_{90} deserve future work.

The real system is more complex than the simplest case we discussed above, because there is orientation distribution in the hex-cyl grains. However, in each grain there are the three directions of the (100) planes along which hex-cyl is transformed into the lamella through the OOT. If the rate R for moving ∇T is slow enough, one of the lamellar orientations with their lamellar normal $\mathbf{n}_l$ being oriented most closely to the ∇T axis has the fastest growth along the ∇T axis and hence dominates the other two orientations, giving rise to the ∇T-field-induced preferential orientation of lamellae.

4.2.4. Difference of the zone-heating-induced lamellar orientation between sheets 1 and 2

The difference of the lamellar orientation attained in those two sheets is clarified in Figs. 8, 9, and 11. The results clearly indicate that the difference is due to the difference in the orientation distribution of hex-cyl with respect to the ∇T direction. Note that the sheets 1 and 2 are identical except for the rotation of the film normal $\mathbf{n}$ by 90°. The orientations of the hex-cyl in the sheets 1 and 2 are schematically illustrated in Fig. 14a and b, respectively. In the as-cast film, the cylinder axis tends to be oriented perpendicular to $\mathbf{n}$ as mentioned in Section 3.1 with two rotational freedoms: One is the rotational freedom of the cylinder axis with respect to $\mathbf{n}$ as shown by the angle ϕ (part a). Another is the rotational freedom of the hexagonal lattice around the cylinder axis as shown by the angle η (part a). In sheet 1, the (100) planes become perpendicular to $\mathbf{n}$ at $\eta = 0°$, while (110) planes are perpendicular to $\mathbf{n}$ at $\eta = 30°$.

The difference in the orientation factor f of the lamellae in between the zone-heated sheets 1 and 2 will be primarily attributed to a difference in the fraction of the (100) plane of hex-cyl oriented normal to the ∇T axis in between the sheet 1 and sheet 2 (see Fig. 14). Furthermore, this difference in the fraction may be estimated by comparing the integrated intensity of the (100) diffraction peak with respect to q and in a narrow sector centered at

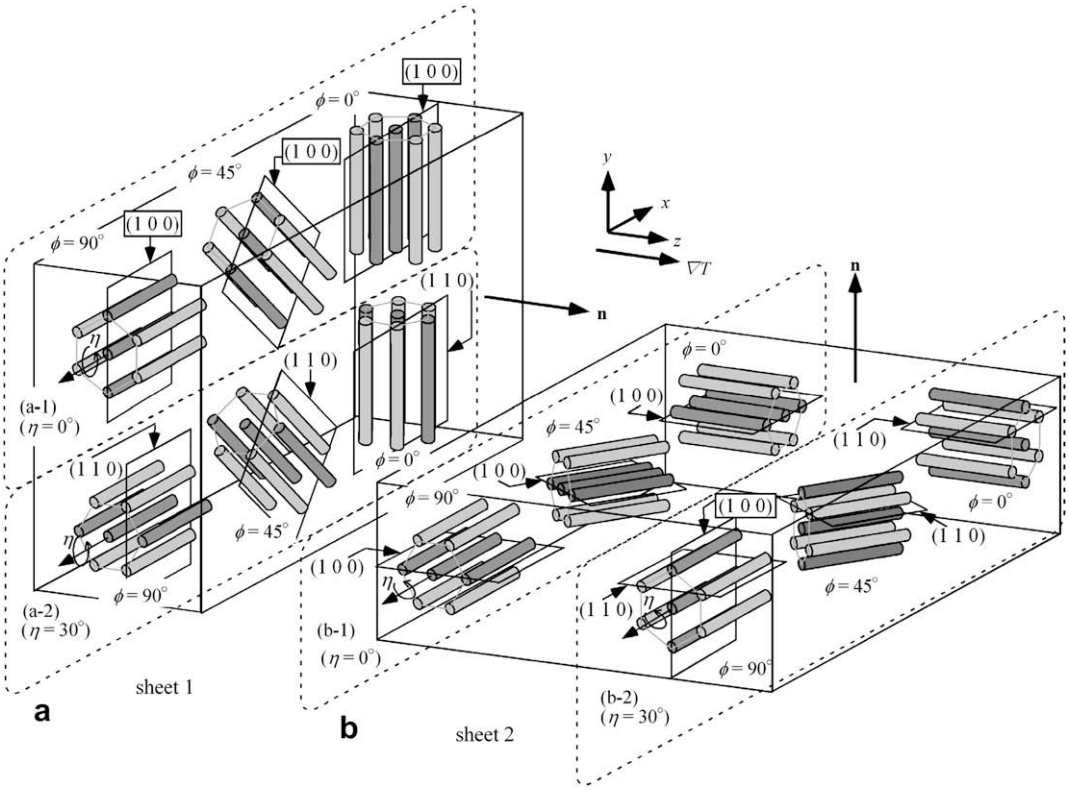

Fig. 14. Schematic illustrations indicating the orientation of the hex-cyl in the sheet 1 (a) and sheet 2 (b) with respect to ∇T axis, and the definition of the rotational angle ϕ and η (a and b). The population of the hex-cyl having (100) planes perpendicular to ∇T direction is larger in the sheet 1 than that in the sheet 2.

$\mu = 0°$ ($|\mu| < \Delta\mu$) for the sheet 1, $\beta_{1,(100)}$, and that at $\mu = 90°$ ($|\mu - 90°| < \Delta\mu$) for the sheet 2, $\beta_{2,(100)}$. The ratio was estimated to be given by $\beta_{1,(100)}/\beta_{2,(100)} = 1.6$, for $\Delta\mu = 5°$.

The fact that the ratio $\beta_{1,(100)}/\beta_{2,(100)}$ is larger than 1 is intuitively obvious from the following reason. In the sheet 1, if $\eta = 0°$, hex-cyl has (100) planes perpendicular to the ∇T direction irrespective of ϕ. On the other hand, in the sheet 2, the (100) planes become perpendicular to the ∇T direction only when the conditions of $\phi = 90°$ and $\eta = 30°$ are satisfied. Thus, the sheet 1 has a larger population of the (100) planes, which are oriented perpendicular to ∇T direction, than the sheet 2, hence resulting in a better alignment of lamellae with respect to the ∇T direction lamella in the zone-heated sheet 1 than in the zone-heated sheet 2, in agreement with the experimental results on *f*.

5. Concluding remarks

The OOT process from hex-cyl to lamella in a given hex-cyl grain produces the three differently oriented lamellae. Hence the OOT processes occurring in many grains of hex-cyl having some orientation distributions tend to further broaden the orientation distribution of the resulting lamellae. However when the OOT process is induced under the zone-heating field, the moving ∇T field across the OOT temperature was found to produce the preferential orientation of lamellae with their lamellar normals oriented along the ∇T axis. We propose that the preferential orientation may be a consequence of the ∇T field selecting the growth of one of the three lamellae with their lamellar normals most closely oriented with the ∇T axis for each hex-cyl grain. The better orientation of the zone-heating-induced lamellar orientation may be attained by an increasing initial orientation of hex-cyl as detailed in the text, by the increased mobility of the bcps which can be induced by an elevated zone-heating temperature for a given molecular weight of SI bcp and for a given moving rate *R*. The research along this line deserves future works.

Acknowledgements

The SAXS measurements in this work were conducted under approval of the Photon Factory Advisory Committee (2002G085, 2004G070, and 2007G100).

References

[1] Anthony RW. Solid state chemistry and its application. New York: John Wiley & Sons Inc.; 1984.
[2] Hashimoto T, Bodycomb J, Funaki Y, Kimishima K. Macromolecules 1999;32:952–4.
[3] Bodycomb J, Funaki Y, Kimishima K, Hashimoto T. Macromolecules 1999;32:2075–7.
[4] Mita K, Tanaka H, Saijo K, Takenaka M, Hashimoto T. Macromolecules 2007;40:5923–33.
[5] Mita K, Tanaka H, Saijo K, Takenaka M, Hashimoto T. Macromolecules 2008;41:6780–6.
[6] Fredrickson GH, Helfand E. J Chem Phys 1987;87:697–705.
[7] Fredrickson GH. Macromolecules 1987;20:2535–42.
[8] Fredrickson GH, Helfand E. J Chem Phys 1988;87:5890–7.
[9] Menelle A, Russel TP, Anastasiadis SH, Satija SK, Majkrzak CF. Phys Rev Lett 1992;68:67–70.
[10] Lambooy P, Russel TP, Kellogg GJ, Mayes AM, Gallagher PD, Satija SK. Phys Rev Lett 1994;72:2899–902.
[11] Koneripalli N, Singh N, Levicky R, Bates FS, Gallagher PD, Satija SK. Macromolecules 1995;28:2897–904.
[12] Binder K. Acta Polym 1995;46:204–25.
[13] Berry BC, Bosse AW, Douglass JF, Jones RL, Karim A. Nano Lett 2007;7:2789–94.
[14] Inoue T, Soen T, Hashimoto T, Kawai H. J Polym Sci A-2 1969;7:1283–302.
[15] Kawai H, Hashimoto T, Miyoshi K, Uno H, Fujimura M. J Macromol Sci Phys 1980;B17:427–72.
[16] Mori K, Hasegawa H, Hashimoto T. Polymer 1990;31:2368–76.
[17] Sakurai S, Momii T, Taie K, Shibayama M, Nomura S, Hashimoto T. Macromolecules 1993;26:485–91.
[18] Pakula T, Saijo K, Kawai H, Hashimoto T. Macromolecules 1985;18:1294–302.

[19] Khandpur AK, Förster S, Bates FS, Hamley IW, Ryan AJ, Bras W, et al. Macromolecules 1995;28:8796–806.
[20] Förster S, Khandpur AK, Zhao J, Bates FS, Hamley IW, Ryan AJ, et al. Macromolecules 1994;27:6922–35.
[21] Amemiya Y, Wakabayashi K, Hamanaka T, Wakabayashi T, Matsushita T, Hashizume H. Nucl Instrum Methods 1983;208:471–7.
[22] Suehiro S, Saijo K, Seto T, Sakamoto N, Hashimoto T, Ito K, et al. J Synchrotron Radiat 1996;3:225–30.
[23] Tanaka H, Hasegawa H, Hashimoto T. Macromolecules 1991;24:240–51.
[24] In Fig. 4c, the higher order broad peaks, e.g., the peak numbered 3 with the thick open arrow for the profile obtained at $\mu = 0^\circ$, the peak numbered 2 at $\mu = 90^\circ$ and the peak numbered 2 for through view, are essentially unaffected by the lattice factor. Hence these peaks essentially reflect the third-order (the peak numbered 3) or second-order form factor peak (the peak number 2), from which we can estimate r_i by using Eq. (1). The lower-order form factor peak positions estimated from thus evaluated r_i and Eq. (1) (the peaks numbered 1 and 2 for the profile at $\mu = 0^\circ$, and the peak numbered 1 for the profile at $\mu = 90^\circ$ or for the through view profile) are consistent with the observed peak positions, though these broad peaks are modulated by the peaks due to the lattice factor.
[25] Hashimoto T, Nagatoshi K, Todo A, Hasegawa H, Kawai H. Macromolecules 1974;7:364–73.
[26] Shibayama M, Hashimoto T. Macromolecules 1986;19:740–9.
[27] Hashimoto T. Macromol Symp 2001;174:69–83.
[28] Hashimoto T, Sakamoto N, Koga T. Phys Rev E 1996;54:5832–5.
[29] Sakamoto N, Hashimoto T. Macromolecules 1998;31:3292–302.
[30] Sakamoto N, Hashimoto T. Macromolecules 1998;31:3815–23.
[31] Schrader D. In: Brandrup J, Immergut EH, Grulke A, editors. Polymer handbook. 4th ed. New York: John Wiley & Sons Inc.; 1999. p. V-91.
[32] Furuta I, Kimura S, Iwama M. In: Brandrup J, Immergut EH, Grulke A, editors. Polymer handbook. 4th ed. New York: John Wiley & Sons Inc.; 1999. p. V-5.